Earth Planets Space, **59**, 523–539, 2007

Evidence for an elevated 410 km discontinuity below the Luzon, Philippines region and transition zone properties using seismic stations in Taiwan and earthquake sources to the south

C. Wright and B.-Y. Kuo

Institute of Earth Sciences, Academia Sinica, P.O. Box 1-55, Nankang, Taipei, Taiwan 11529

(Received May 22, 2006; Revised October 24, 2006; Accepted March 12, 2007; Online published June 27, 2007)

P waves from earthquakes south of Taiwan, recorded by seismic stations within and around Taiwan, were used to define two average wavespeed models WPSP01 and WPSP02 for the upper mantle and transition zone below the Luzon region. Wavespeeds are characteristic of oceanic upper mantle. The 410-km discontinuity, however, appears to be elevated to about 325 km depth, based on clear identification of the travel-time branch produced by refraction within the transition zone, and estimates of its first and second derivatives with respect to distance. A plausible explanation is low temperatures within the subducted South China Sea plate. The data also imply relatively low wavespeed jumps of 0.6–1.0% and 1.1–1.5% respectively across the elevated 410-km discontinuity and a lower discontinuity at 676 km depth, and high wavespeed gradients in the transition zone. Phase-weighted stacking on a cluster of short-period seismograms with first arrival energy from within the transition zone provides independent support for the validity of the models; later arrivals are detected close to the predicted times and slownesses for energy emerging from the lowermost upper mantle and the top of the lower mantle. An additional arrival on the stacks may be caused by a localized discontinuity near 530 km depth.

Key words: Philippine Sea plate, Luzon, upper mantle, transition zone.

1. Introduction

The existence of two major discontinuities at depths of about 410 and 660 km that define the top and bottom of the transition zone was established over 40 years ago (Niazi and Anderson, 1965). Since that time, numerous studies of this region have been published, often using refracted *P* waves (e.g. Simpson *et al*, 1974; Walck, 1984; Kaiho and Kennett, 2000; Kato and Nakanishi, 2000; Simon *et al*., 2002), sometimes refracted *S* waves (e.g. Ibrahim and Nuttli, 1967; Simon *et al*., 2003) or surface waves (e.g. Anderson and Toksöz, 1963), whilst more recent studies include the use of *P*-to-*SV* or *SV*-to-*P* conversions of upgoing seismic body waves at the discontinuities, *ScS* reverberations, and precursors to *PP* and *SS* phases (e.g. Vinnik, 1977; Revenaugh and Jordan, 1991; Shearer and Flanagan, 1999; Li *et al*., 2000). While these discontinuities have been explained in terms of the phase transformations expected in olivine, pyroxenes and garnets (Ringwood, 1991), there are still difficulties in reconciling the wavespeed and density models obtained from seismology with the properties of the mineral phases established from experimental petrology and mineral physics (Anderson and Bass, 1984; Bass and Anderson, 1984; Fujisawa, 1998; Nishihara and Takahashi, 2001; Bass and Schilling, 2003). Moreover, there are still many regions of the earth, especially in oceanic regions, for which knowledge of the structure of the upper mantle and transition zone is poor. Estimates of the wavespeed and density changes across the discontinuities are often poorly resolved, and accurate definition of wavespeed gradients within the transition zone has rarely been obtained.

Two possible petrological models for the upper mantle and transition zone are debated. The more widely accepted olivine-rich pyrolite model (Ringwood, 1962, 1991; Fujisawa, 1998) explains the overall density change across the transition zone, but does not provide good agreement with either the estimated wavespeed change across the 410 km discontinuity or the wavespeed gradients within the transition zone (Duffy and Anderson, 1989; Duffy *et al*. 1995; Li *et al*., 1998). Several authors have argued that the alternative pyroxene- and garnet-rich piclogite model (Anderson and Bass, 1984; Bass and Anderson, 1984) explains the observed seismic properties within and adjacent to the transition zone as well as the pyrolite model (Duffy and Anderson, 1984; Ita and Stixrude, 1992; Nishihara and Takahashi, 2001). Considerable uncertainty therefore still remains in using models from seismology to constrain mantle properties and composition.

While the two major discontinuities at about 410 km and 660 km depth are widespread over most of the earth, variations in depths and properties due to the localised lower temperatures and more mafic compositions of subduction zones have been identified. In subduction zones, phase transformation boundaries and mineral assemblages may differ due to the presence of water as well as differences in temperature and composition from the surrounding mantle (Okamoto and Maruyama, 2004). In cold, subducting

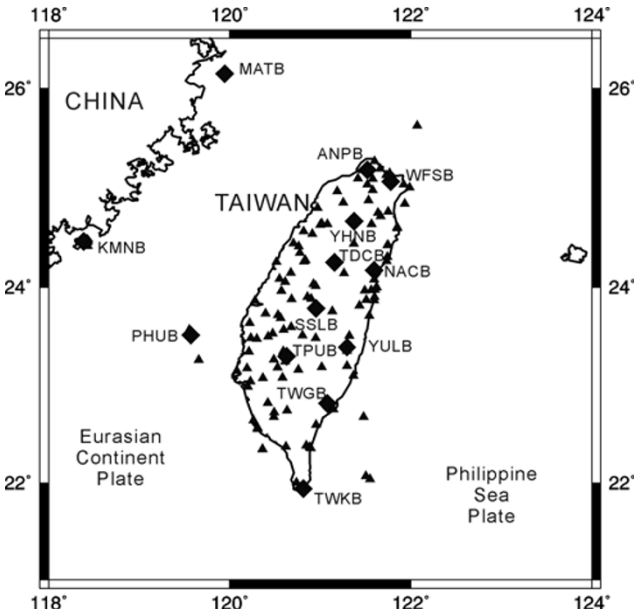

Fig. 1. Map showing stations used in the present study. Diamonds signify broad-band stations of the BATS array, and triangles short-period stations of the CWB network.

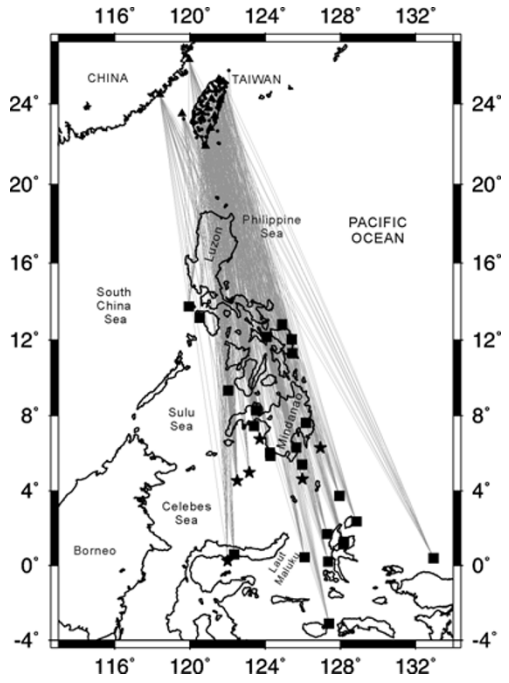

Fig. 2. Map showing distribution of events used to determine mantle structure, with great circle paths (dotted grey lines) to the stations providing seismograms for each event. Squares and stars denote events at depths of 150 km or less and depths greater than 150 km, respectively.

slabs in which thermodynamic equilibrium has occurred, the olivine-β phase-spinel phase boundaries may be elevated (positive Clapeyron slope or exothermic reaction) while the 660 km discontinuity may be depressed (negative Clapeyron slope or endothermic reaction) (Li *et al*., 2000). Numerical modelling studies that use the properties of the olivine-β phase-spinel phase boundary as part of the process of calculating the stress regime and depths of phase transformations in subducting slabs (Schmeling *et al*., 1999; Negredo *et al*., 2004), predict that the depth of the 410 km discontinuity may be elevated by 70 km or more. Seismological observations have been used to estimate a 60 km elevation of the olivine-β phase-spinel boundary in the Izu-Bonnin subduction zone (Collier and Hellfrich, 1997), a smaller elevation of 20 km has been reported in a continental region (Chen *et al*., 1997), and other examples are given in Wright (2007).

The 660 km discontinuity is known to be anomalously deep around some subduction zones (Li *et al*., 2000). For *P* waves, the discontinuity is also poorly defined below parts of southern Africa (Zhao *et al*., 1999; Simon *et al*., 2002) and apparently absent below the Himalayan region (Ram and Mereu, 1977), suggesting that the properties of the lower part of the transition zone may vary regionally away from those regions where subduction is currently taking place.

The aim of this work is to derive average *P* wave models of the upper mantle and transition zone beneath the western margin of the Philippine Sea plate around Luzon. Emphasis is on the seismological evidence to explain the travel-time anomalies that exist in the region, which was previously studied by Nowack *et al*. (1999). The geodynamic consequences of the results are explored by Wright (2007). Earthquakes recorded by the broad-band BATS array (Broad-band Array in Taiwan for Seismology) and the short-period CWB (Central Weather Bureau) seismic network (Fig. 1) provided refracted arrivals to define mantle structure between depths of 100 and 800 km. An important focus of the work, due to limitations of the available data, is on the information on structure provided by travel-time measurements. Such data provide constraints on the depths of major discontinuities, the wavespeed changes across discontinuities and wavespeed gradients within the transition zone. The models have been tested by stacking seismograms to identify later arrivals associated with the triplications produced by the inferred discontinuities. Further refinements, to be explored in a later paper, involve the comparison of the signal waveforms with synthetic seismograms, and the development of complex, laterally-varying and frequency-dependent earth models for the region around Taiwan, which rely on the initial development of a robust one-dimensional model.

2. Selection of Data

The distribution of seismicity around Taiwan suggests the construction of three roughly linear profiles to examine the structure of the upper mantle and transition zone in the region: to the north-east along the Ryukyu arc (azimuths 30°–60° from central Taiwan), to the south along the western margin of the Philippine Sea plate (azimuths 150°–190°) and possibly a more diffuse profile to the west across eastern Asia (azimuths 260°–305°). The present work is concerned with the second of these profiles to the south of Taiwan.

The BATS array consists of 14 broad-band instruments (Streckheisen three-component STS 2 seismometers, except for TDCB and TWKB which have Streckheisen STS 1 seismometers) deployed in Taiwan, on nearby islands, or

Table 1. Earthquakes used for determining mantle structure.

No.	Date	Event Lat. °N	Event Long. °E	O.T. (GMT)	Depth (km)	M#	No. of stations providing data		Epicentral distance range (deg)	Azimuth from station (deg)	Corrected distance (deg)
							BATS	CWB			
1.	01/01/2002	6.30	125.65	11-29-22.73	138	5.9	10		16.23–20.48	157.7–167.5	17.80–21.91
2.	05/03/2002	6.03	124.25	21-16-09.13	31	6.3	10		16.96–20.43	161.9–172.5	17.18–20.64
3.	08/03/2002	5.87	124.27	18-27-53.19	23	5.6	11		16.32–20.59	162.0–172.5	16.47–20.73
4.	21/12/2002	4.98	123.16	17-41-13.54	602	5.4	10		17.01–21.28	165.9–175.3	24.10–27.94
5.	30/12/2002	7.47	123.41	04-49-08.69	10	5.9	10		15.43–18.87	163.3–173.8	15.49–18.94
6.	15/02/2003	12.17	124.08	11-01-59.86	10	5.8	13		10.20–14.45	155.2–170.0	10.29–14.54
7.	10/03/2003	1.69	127.30	02-09-37.08	93	6.2	13		21.09–25.33	157.8–166.3	21.98–26.12
8.	14/03/2003	0.41	132.95	07-06-13.31	33	6.0	13		25.17–29.24	148.1–155.3	25.34–29.40
9.	16/04/2003	0.25	122.01	09-31-23.94	192	5.2	11		21.59–24.80	171.1–179.5	23.11–26.28
10.	27/04/2003	5.41	125.98	16-08-42.03	137	5.3		11	17.58–18.79	162.5–165.1	19.09–20.26
11.	05/05/2003	0.22	127.35	15-50-08.47	123	5.9	13		22.51–26.76	158.8–166.9	23.42–27.64
12.	05/05/2003	3.72	127.95	23-04-45.67	56	6.0	13		19.39–23.60	154.4–163.4	19.88–24.04
13.	22/05/2003	11.30	125.46	17-45-37.63	71	5.4	7		11.47–15.67	151.6–165.1	14.45–16.76
14.	26/05/2003	2.35	128.85	19-23-27.94	31	6.5	12		20.98–25.17	153.7–162.1	21.14–25.33
15.	26/05/2003*	6.76	123.71	23-13-29.72	565	6.2	12	63	15.33–19.62	162.9–175.0	21.79–25.83
16.	12/06/2003	13.17	120.51	18-43-32.73	46	5.6	7		9.61–11.42	169.4–185.6	11.10–12.72
17.	01/07/2003	4.53	122.51	05-52-25.92	635	5.8	12	45	17.38–21.65	168.0–178.8	25.11–28.86
18.	01/07/2003	12.80	124.90	17-00-22.82	33	5.6	13		9.88–14.08	150.8–165.9	10.23–14.42
19.	11/07/2003	9.34	122.04	13-53-24.90	33	5.6	13		12.58–16.85	166.3–179.1	12.92–17.19
20.	11/08/2003	1.14	128.15	00-19-09.28	10	5.7	13		21.87–26.10	156.3–164.6	21.93–26.14
21.	11/08/2003	1.26	128.19	00-22-26.40	10	5.5	8		21.79–24.48	159.7–164.4	21.84–24.53
22.	02/10/2003	4.62	125.98	23-24-05.75	154	5.0	8	27	17.93–22.18	158.4–167.6	19.64–23.72
23.	09/10/2003	13.76	119.94	22-19-13.85	33	5.7	13		8.18–12.34	171.9–189.1	8.52–12.68
24.	18/10/2003	0.44	126.10	22-27-13.25	33	6.1	11		21.98–26.24	161.4–169.7	22.15–26.41
25.	18/11/2003	12.02	125.42	17-14-22.62	35	6.1	13		10.79–14.97	150.4–164.5	11.16–15.31
26.	28/12/2003	0.60	122.35	05-36-54.81	74	5.4	10		21.26–25.51	170.2–178.1	21.77–26.01
27.	28/01/2004	−3.12	127.40	22-15-30.70	17	6.0	12		25.72–29.98	161.0–168.2	25.81–30.06
28.	29/01/2004	6.29	126.94	09-48-42.76	209	5.7	12		16.64–20.85	154.1–164.4	19.14–23.11
29.	26/02/2004	8.29	123.52	17-25-56.19	12	5.2	9		13.82–18.09	162.2–174.1	13.93–18.18
30.	16/05/2004	7.63	126.17	11-01-14.52	11	5.7	11		15.13–19.35	154.7–165.7	15.23–19.42
					Total		323	146			
31.	10/06/2004+	55.68	160.00	15-19-57.75	189	6.9	12		41.32–44.46	30.7–33.5	42.55–45.64

#Event magnitude.
*ScP times also picked for estimating station corrections.
+Teleseismic event—times used for estimating station corrections.

on islands close to mainland China (Fig. 1). The array is run by the Data Management Centre, Institute of Earth Sciences (IES), Academia Sinica, and the data are telemetered by radio to the IES building in eastern Taipei. Records from 30 earthquakes at distances between 8° and 30°, azimuths between 150° and 190°, and magnitudes greater than 5.0 recorded at stations of the BATS array were selected from the data base of the Institute of Earth Sciences, Academia Sinica, for the years 2002–2004 (Fig. 2 and Table 1). Data were recorded at 20 Hz sampling rate and preliminary processing undertaken using SAC (Seismic Analysis Code) software for 13 of the stations; one station, LYUB, was too noisy to give useful data.

While the BATS array provides high-quality broad-band records, the denser CWB network, equipped with Teledyne-Geotech S-13 short-period seismometers, whose function is to provide information on local seismicity, may provide additional constraints on deep structure, and was previously used for this purpose by Nowack *et al*. (1999). Records were extracted from the CWB database by staff of the Institute of Earth Sciences, Academia Sinica, and archived at a 100 Hz sampling rate for later processing using SAC. 4 events were selected to determine how effective the data would be in supplementing the BATS data for defining the structure of the upper mantle and transition zone (Table 1), and provided data from 63 of the 75 stations of the network. Records from earthquakes outside the Taiwan region are discarded from the CWB database about 12 months after their occurrence, unless researchers arrange to save them. The amount of data from CWB stations currently available for this kind of study is therefore limited.

3. Methods of Data Analysis

3.1 Character of seismograms

The approach to analyzing the data was influenced by two factors: the sparse distribution of broad-band stations which require an emphasis on deriving a model that represents an average structure over the region studied, and the complexity of the seismograms. To illustrate this complexity, a record section for 11 stations from the BATS array and 10 stations from the CWB network for an earthquake south west of Mindanao (event 28 of Table 1) is shown in

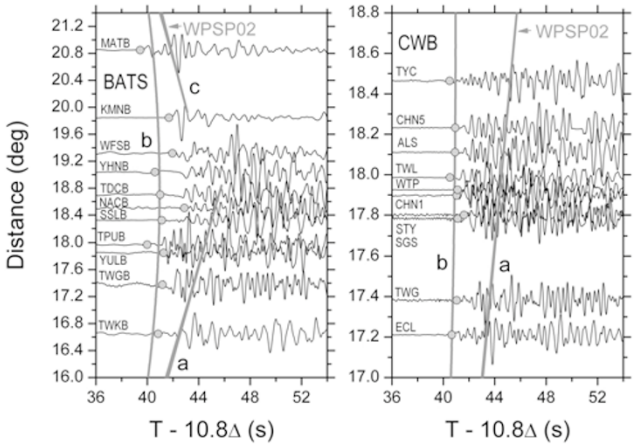

Fig. 3. Seismograms for event 28 of Table 1 at 11 BATS stations (left) and 10 CWB stations used to construct phase-weighted stacks plotted as epicentral distance against reduced travel time. Station corrections (Fig. 4) were applied prior to plotting. Data from the BATS stations were used in deriving models WPSP01P and WPSP02P, whilst data from the CWB stations were used only for generating phase-weighted stacks. The travel-time curve computed from model WPSP02 has been superimposed after applying a 'baseline' shift of 0.92 s (the 'event bias correction' for the event). Travel-time branches 'a', 'b' and 'c' are labelled, and explained in the caption to Fig. 5. Because the event was at a depth of 209 km, the cross-over point between branches 'a' and 'b' at 17.7° distance for an event on the surface has been shifted back to 14.2°.

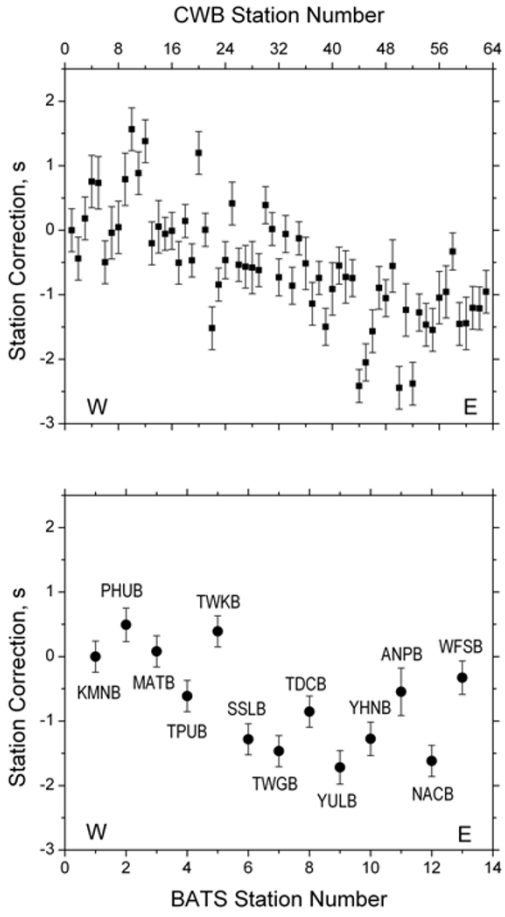

Fig. 4. Station corrections for CWB (top) and BATS stations (bottom), with stations arranged from west to east.

Fig. 3. All data were filtered with a bandpass of 0.4–5.0 Hz, which makes the waveforms of adjacent BATS and CWB stations very similar. The seismograms from CWB stations for this event were not used in deriving the wavespeed models, and were chosen as good examples for presentation because they have clear arrivals from a fairly deep event (209 km depth), have energy from the transition zone as the first arrival for all stations, and, with signal processing, yield information on later arrival branches. Circles mark the picked arrival times at the BATS and CWB stations, and all times of onsets and seismograms were corrected using the station corrections of Fig. 4.

The travel-time curve calculated from model WPSP02 (Figs. 5 and 6) is superimposed on the record sections with a time shift of 0.92 s (the 'event bias correction' for the event defined in Section 4). Observed travel times can be divided into three main arrival branches (Fig. 5) denoted 'a' (refracted paths through the upper mantle), 'b' (refracted paths through the transition zone), and 'c' (refracted paths through the lower mantle), with 'b' as the first arrival for all seismograms in Fig. 3. At TWKB and CWB station ECL, there is a strong later arrival that matches branch 'a'. Stations KMNB and MATB have especially clear arrivals due to their location on stable continental crust close to the Chinese mainland. In particular, the *P* wavetrain at MATB shows two clear arrivals that can be attributed to branches 'b' and 'c'. However, for stations on or close to the island of Taiwan, there are large variations in waveform, even at closely-separated stations, due to the complicated underlying lithospheric structure. This makes it difficult to reliably identify the later arrival branches without the careful processing described in Section 6.

3.2 Focal depth and station corrections

Arrival times of the earliest *P* wave arrivals measured on records bandpass-filtered between 0.4 and 5.0 Hz were the primary input data. All distances and times were corrected by ray tracing to make each event appear to be located on the surface. The slownesses used for making the corrections were derived from the IASPEI 1991 Seismological Tables (Kennett, 1991), and the IASP91 *P* wavespeed model from the tables was adopted for the ray tracing. An important step in the interpretation was to ensure that each arrival time was attributed to the correct travel-time branch 'a', 'b' or 'c' prior to making the correction. Errors in the corrected distances and bias in slowness due to the differences between the local structure and the reference model are small (see Section 9). However, errors in the total travel times, which can be significant if an inappropriate reference model is chosen, are largely eliminated later by absorption into the 'event bias corrections'.

The structure of the crust and uppermost mantle below Taiwan is complex, shows strong lateral variations, and variations in Moho depth are still poorly known (Ma *et al.*, 1996; Chen *et al.*, 2004; Kim *et al.*, 2004). Scatter of the measured times is considerable and strongly influenced by structure below the stations. The decision was made to correct for this effect by deriving station corrections, rather than by applying ray tracing through a com-

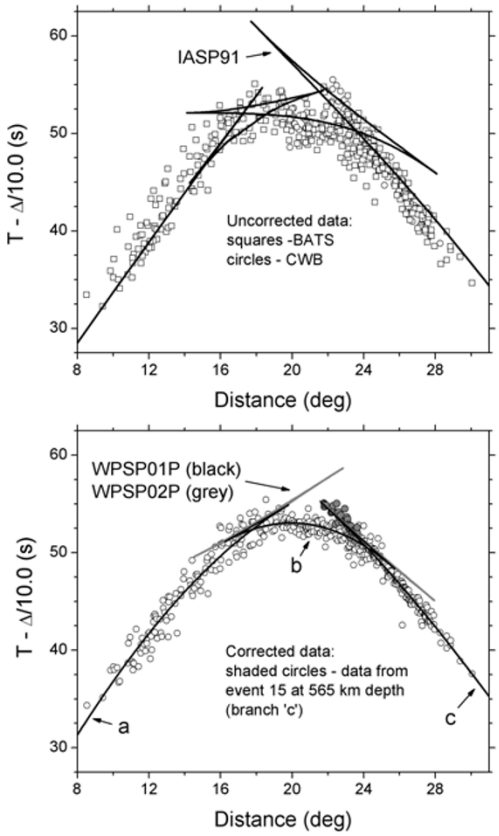

Fig. 5. (Top) Reduced travel-time curve for the IASP91 model of Kennett (1991), with measured first arrival times adjusted to their surface-to-surface equivalents; (bottom) surface-to-surface times with both station corrections and 'event bias corrections' applied, and curve fits for branches 'a' (refracted arrival from the upper mantle), 'b' (refracted arrival from within the transition zone) and 'c' (refracted arrival from within the lower mantle). Travel times computed from models WPSP01P and WPSP02P are superimposed on the estimated travel-time branches to show how well the model-generated times fit the data.

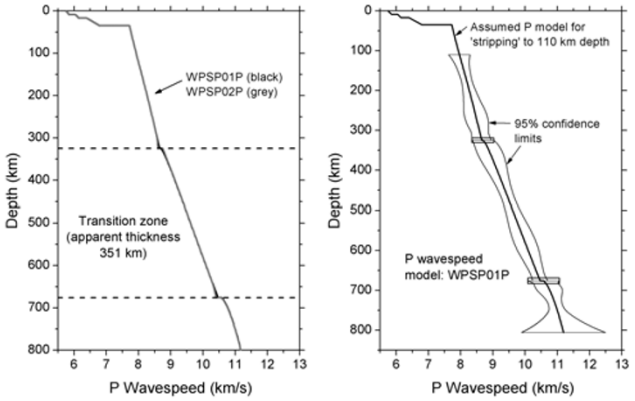

Fig. 6. (Left) *P* wavespeed models WPSP01P and WPSP02P; (Right) *P* wavespeed model WPSP01P with 95% confidence limits on wavespeed estimates.

plex three-dimensional model assembled from earlier studies, whose reliability would be difficult to assess. The procedure involved first calculating the travel-time residuals relative to the arrival times predicted from the IASP91 model (Kennett, 1991) for times attributed to branch 'c' (i.e. arrivals from signals that had penetrated to lower mantle depths). Figure 5 shows the travel-time curves calculated by ray tracing for a surface event recorded at locations on the surface using the IASP91 model (top) and the models derived in this study (bottom). Significant distance-dependent differences in earth structure from those of the reference model (IASP91) are assumed to be absent from time measurements of branch 'c' that were first arrivals. With this assumption, 5 events (events 4,8,15,17 and 27 of Table 1) were available to provide estimates of station corrections. The data were supplemented by times from one teleseism (last event in Table 1) and the *ScP* times from event 15.

A least-squares inversion was then performed to estimate a station correction for each of the 13 stations of BATS and a 'bias' term for each earthquake, consisting of the combined errors in origin time and correction for focal depth, and the effect of real deviations in earth structure from the reference model. Two separate bias terms were calculated for event 15, because the *P* and *ScP* arrivals travelled different paths, and therefore the effects of deviations from the reference model were unrelated. This resulted in 83 observations for estimating 20 parameters. Because the observations used in the least-squares inversion consisted of differences between the parameters that were being estimated, one parameter (the station correction for KMNB near the Chinese mainland) was set to zero. KMNB was chosen because it is a reliable station away from the structural complexities of Taiwan, and is also the reference station used by Chen *et al.* (2004). The station corrections and estimated standard errors are plotted in the lower half of Fig. 4, noting that the estimated standard deviation on a single difference between a station correction and an event 'bias', σ, was 0.64 s. As a check, the inversion was also undertaken for the remaining times belonging to branches 'a' and 'b' (264 observations for estimating 37 parameters), although complex deviations from the reference model were clearly present, making good agreement with the earlier results unlikely. Nevertheless, satisfactory agreement with the results of Fig. 4 was obtained for 9 of the 13 stations, but the standard deviation, σ, increased to 1.14 s.

A similar analysis was also undertaken for the three events recorded by CWB stations that gave times for branch 'c', supplemented by the *ScP* times for event 17 (209 observations for estimating 67 parameters, 63 of them station corrections). Despite the large number of stations and relatively small number of observations, the station corrections at CWB stations at locations within 10 km of a BATS station were in satisfactory agreement with their BATS counterparts (Table 2). Furthermore, the general regional trend of CWB station corrections shown in the upper part of Fig. 4 was in satisfactory agreement with the results from BATS, while the standard deviation, σ, was 0.57 s.

4. Corrections for Errors in Origin Times (Event-bias Corrections)

To derive a regional travel-time curve, corrections must be made for errors in both earthquake origin times and the time corrections for focal depth, which are called 'event bias corrections'. The 'event bias corrections' defined here differ in one important respect from the estimates of com-

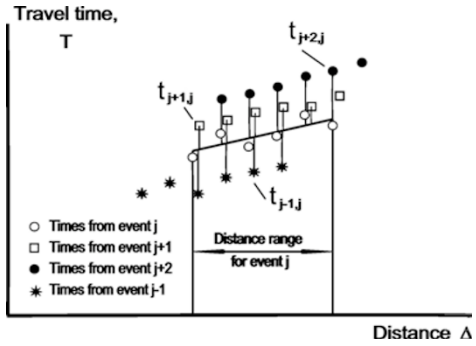

Fig. 7. Method of determining 'event bias corrections'.

Table 2. Comparison of station corrections at BATS and CWB stations separated by less than 10 km.

BATS station	Station correction, s	CWB station	Station correction, s
KMNB*	0.00 ± 0.24	KMN	0.00 ± 0.33
TDCB	-0.85 ± 0.24	TWT	-0.55 ± 0.29
TPUB	-0.61 ± 0.24	WTP	-0.47 ± 0.26
TWGB	-1.47 ± 0.24	TWG	-1.50 ± 0.29
TWKB	0.39 ± 0.24	TWK1	0.39 ± 0.29
WFSB	-0.33 ± 0.26	NWF	-1.45 ± 0.41
YHNB	-1.28 ± 0.26	NSK	-1.57 ± 0.33
YULB	-1.72 ± 0.26	TWF1	-2.42 ± 0.26

*For stations KMNB and KMN, the station corrections were set to zero, as described in the section on the least-squares inversion.

bined errors in origin times and corrections for focal depth that were used for separating station corrections. The input times have already been corrected for station effects, and the new set of corrections are estimated independently of any reference travel-time curve. The principle of the method is illustrated in Fig. 7.

The first step was to fit a separate line or a quadratic polynomial through the arrival times from each of the 30 earthquakes used, adjusted to correspond to surface-to-surface paths. A quadratic form was used only if there was an improvement in fit (10 % reduction in standard deviation on time residuals) over the linear form. To check the value of using station corrections, the curve fitting was undertaken using times from both BATS and CWB stations first with, and then without application of station corrections. The application of station corrections resulted in improved fits for 22 of the 30 events, with the worse fits concentrated at short distances where the scatter of the times is greatest. There is a gradual decrease in the standard deviation on the time residuals on the curve fits to the times with station corrections for each event from about 1.5 s at the shortest distances to about 0.6 s on average for the times on branch 'c' at the largest distances, indicating less effects of inhomogeneity as the seismic energy travels deeper paths. The results therefore showed the necessity of undertaking all computations on times with the station corrections applied.

After the curve fitting, the following procedure was used for deriving 'event bias corrections'. Consider the curve fit to the times for a particular earthquake j (Fig. 7). Time residuals from all other earthquakes relative to this curve, for which seismograms lie within the distance range of the stations recording this earthquake, were used to calculate an average residual for each event, provided that at least two stations were within this distance range. This is represented in Fig. 7 by the times $t_{j-1,j}$, $t_{j+1,j}$ $t_{j+2,j}$, which define the average time residuals from earthquakes $j-1$, $j+1$ and $j+2$ relative to a reference event j. This process was repeated using all earthquakes as the reference event, and the average residuals provided input data to estimate relative origin time errors using a weighted least-squares inversion procedure; the weight for each average residual was the number of degrees of freedom ($n-1$, where n is the number of residuals used to compute the average). The method was previously used by Simon *et al*. (2002) and Wright *et al*. (2002), and the mathematical details provided by Wright (2006).

The 'event bias corrections' are reliably-determined parameters having standard errors in the range 0.07–0.21 s. Because the inversion is undertaken on differences, one earthquake has to be taken as a reference, and its correction set to zero. Event 17 of Table 1 was chosen as the reference, since it provided clear arrivals at both the BATS array and CWB network, with all times belonging to branch 'c' of Fig. 5. After applying station corrections, taking both KMNB (BATS) and KMN (CWB) (7.6 km from KMN) to have values of zero (Table 2), the mean travel-time residual of this event relative to the IASPEI travel times was 0.67 s. Since the travel-time residuals on the times for all events relative to IASPEI are, on average, slightly earlier for branch 'c' at larger distances (Fig. 5), and become progressively later as the distance decreases along branches 'b' and 'a', no further refinement of the choice of reference time can be made. Later observed times relative to the IASPEI times at short distances are expected for any region of oceanic mantle, since the reference times were generated by a model that is a weighted average of oceanic and faster continental wavespeeds.

After applying the 'event bias corrections', the new set of travel times used to derive models had the following properties: (i) corrected for errors in origin times, in time corrections for focal depth, and for station effects, but uncertain by a constant which was defined to give times at 28° distance, slightly later than the IASPEI times; (ii) defined independently of any reference travel-time curve, apart from the tie to IASPEI times at 28°. The accuracy of the long-wavelength variations in these travel times depends on the density of travel-time measurements, the amount of overlap in distance range of the events, and the amount of lateral heterogeneity over the region studied. The application of 'event bias corrections' also suppresses any time anomalies produced at shallow depths in the source region. Cumulative errors in 'event bias corrections' between distances of 8.5° and 30.0° are estimated to be less than one second. The physical basis and significance of the 'event bias corrections' are discussed further in Appendix B.

5. Construction of a Preliminary Earth Model

The travel times of Fig. 5 are divided into three main first arrival branches 'a', 'b' and 'c' with intersection points at distances of 17.7° (a-b) and 24.2° (b-c) for surface-focus

Table 3. Definition of travel-time branches 'a', 'b' and 'c'.

Branch	Polynomial coefficients		No. of data points	Distance range (deg)	Standard deviation (s)
a	2.90399 s (t^0)	15.2855 (t^1)	123	8.52–18.94	1.33
	-7.79730×10^{-2} s^{-1} (t^2)				
b	-2.51117 s (t^0)	16.6843 (t^1)	211	17.10–24.92	0.86
	-9.94385×10^{-2} s^{-1} (t^2)				
c	58.6205 s (t^0)	12.8536 (t^1)	246	21.79–30.06	0.73
	-1.04426×10^{-2} s^{-1} (t^2)				
	7.76591×10^{-4} s^{-2} (t^3)				

Table 4. Preliminary *P* model WPSP02P (Western Margin, Philippine Sea Plate 02—*P* waves) constructed to fit branches 'a', 'b' and 'c'.

Model for 'stripping'		Model from travel-time inversion					
Depth (km)	*P* wavespeed (km/s)	Depth (km)	*P* wavespeed (km/s)	Depth (km)	*P* wavespeed (km/s)	Depth (km)	*P* wavespeed (km/s)
0.0	5.7500	110.0	7.9602	340.0	8.8353	590.0	10.0499
9.0	5.8500	120.0	7.9948	350.0	8.8858	600.0	10.0981
9.0	6.0500	130.0	8.0297	360.0	8.9363	610.0	10.1463
17.0	6.1500	140.0	8.0646	370.0	8.9868	620.0	10.1941
17.0	6.4000	150.0	8.0993	380.0	9.0369	630.0	10.2407
35.0	6.8000	160.0	8.1336	390.0	9.0865	640.0	10.2852
35.0	7.7218	170.0	8.1676	400.0	9.1358	650.0	10.3240
45.0	7.7516	180.0	8.2012	410.0	9.1847	660.0	10.3555
55.0	7.7821	190.0	8.2344	420.0	9.2334	670.0	10.3836
65.0	7.8131	200.0	8.2673	430.0	9.2819	676.0	10.3994
75.0	7.8448	210.0	8.2998	440.0	9.3303	676.0	10.5571
85.0	7.8770	220.0	8.3319	450.0	9.3785	681.0	10.6237
95.0	7.9098	230.0	8.3637	460.0	9.4266	691.0	10.7026
105.0	7.9432	240.0	8.3951	470.0	9.4746	701.0	10.7648
109.6	7.9588	250.0	8.4262	480.0	9.5226	711.0	10.8193
		260.0	8.4571	490.0	9.5705	721.0	10.8688
		270.0	8.4876	500.0	9.6184	731.0	10.9146
		280.0	8.5178	510.0	9.6663	741.0	10.9575
		290.0	8.5458	520.0	9.7142	751.0	10.9979
		300.0	8.5673	530.0	9.7620	761.0	11.0363
		310.0	8.5817	540.0	9.8099	771.0	11.0727
		320.0	8.5934	550.0	9.8578	781.0	11.1075
		325.0	8.5986	560.0	9.9058	791.0	11.1406
		325.0	8.7594	570.0	9.9538	801.0	11.1723
		330.0	8.7847	580.0	10.0018	806.0	11.1877

events. The cross-over distances between the branches were resolvable by visual inspection of the corrected times, but were confirmed by locating the point of inflection of the slowness relation estimated from these times (see Section 9 and figure 3 of Wright *et al*., 1985). Because the location of the nearer cross-over distance is especially important for the definition of the 410-km discontinuity, further discussion is provided in Appendix A. Travel-time curves were fitted to the three branches with a small amount of overlap. The identification of these branches implies the existence of both the 410- and 660-kilometre discontinuities. The branches 'a', 'b' and 'c' were found to be satisfactorily fitted with quadratic, quadratic and cubic polynomials respectively (Fig. 5 and Table 3). Branch 'c' was defined for corrected distances from 21.8°–30.1°, so that the observations extend 2.4° back from the cross-over point for first arrivals through the times for event 15 at a depth of 565 km (Table 1). For this event, branch 'b' was not observed, since the slope of the first arrivals shows that they belong to branch 'c' (Fig. 5). The final models WPSP01 and WPSP02 predict that branch 'b' should be the earliest arrival over part of the distance range of this event. However, failure to observe branch 'b' could have several explanations, including incorrect focal depth and radiation pattern effects, and does not necessarily imply that there is a problem with the final models.

The times start at a (surface-to-surface) distance of 8.5°, so that a model must be adopted to 'strip' the earth to the depth at which adequate resolution of structure is provided by the data. An average model of the structure of the crust and uppermost mantle for the Taiwan region was devised for this purpose, based on previous seismological studies of the region (Ma *et al*., 1996; Nowack *et al*., 1999; Chen *et al*., 2004; Kim *et al*., 2004); it has a crust 35 km thick and a low uppermost mantle wavespeed of 7.72 km/s characteristic of continental crust overlying young, oceanic upper

mantle (Table 4, left two columns). The model provides travel times and slownesses that fit smoothly on to branch 'a' at a distance of 10.0° where the data coverage becomes reasonably dense. This corresponds to a depth of 109.8 km and a wavespeed of 7.959 km/s. The model was used to 'strip' the earth to a depth of 110 km, and the Herglotz-Wiechert integral (Shearer, 1999, pp. 66–67) was used to determine a wavespeed model to a depth of 500 km, by extrapolating the slowness curve of branch 'a' to a distance of 25°. The resulting model was then used to 'strip' the earth to several depths between 320 km and 400 km, and the Herglotz-Wiechert integral undertaken along branch 'b' extrapolated to distances of 26°. For each depth, the starting distance for the new integration was calculated during the stripping process. When the best fit for the depth of the assumed first-order discontinuity had been obtained (325 km), the earth was stripped to that depth and the Herglotz-Wiechert integral evaluated along branch 'b' extrapolated to a distance of 30° to give wavespeed models to depths of about 800 km. The new model was then used to 'strip' the earth to several depths between 640 and 680 km. Herglotz-Wiechert integration was then undertaken along branch 'c' and ray tracing used to select the depth of the discontinuity that gave the best fit to the observed times (676 km). The preliminary model WPSP01P resulting from these computations is shown in Fig. 6.

Model WPSP01P shows small wavespeed jumps across the discontinuities at depths of 325 and 676 km compared with many other published models of the transition zone (0.6% and 1.1% respectively, compared with 3.6% and 5.8% respectively in the IASP91 model of Kennett, 1991, for example). This situation arises because of the measured gradients of branches 'a', 'b' and 'c' in the distance ranges in which they are first arrivals; when these gradients are extrapolated into the region in which they are later arrivals, they imply small wavespeed jumps across both discontinuities. The wavespeed gradients within the transition zone (Fig. 6), which were defined by the first arrivals (corresponding depths 361–608 km) are high compared with many other models. The wavespeed gradients may be lower both above and below the two discontinuities than the derived slowness curves suggest, but the reduced gradients of the branches of the slowness curves would be difficult to estimate from later arrivals. If this were true, the changes in wavespeed at each discontinuity permitted by the travel times would be larger. To test this idea, the slowness curves for branches 'a' and 'b' were changed in the regions in which they were second arrivals to have lower gradients. Slowness curves of branches 'a' and 'b' are defined by linear forms. At the crossover distance of 17.7°, the slowness gradients were reduced by changing to quadratic forms on both the high- and low-distance sides of the cross-over for branches 'a' and 'b' to bend the gradients to lower values over a distance range of 1°, and then return to a linear form. Continuity of both the slowness and its first derivative were imposed. No attempt, however, was made to change the slowness gradient of branch 'c' at distances less than the cross-over at 24.2°, since the gradient was defined by observations in this distance range from event 15 of Table 1. However, the slowness gradient of branch 'b' was reduced at distances greater than 24.2°, where it was a later arrival. The modified slowness curves suggest that the increases in wavespeed across the upper and lower discontinuities can be increased to 1.0% and 1.5% respectively, which are still lower than in many published models, due to the high estimated wavespeed gradients in the transition zone.

6. Identifying Later Branches Associated with Triplications

The broad-band stations of the BATS array are too far apart to allow the effective use of stacking techniques to enhance later arrivals. The alternative is to use the more densely-spaced stations of the short-period CWB network. Finding data of sufficient quality to allow a search for branches 'a' and 'c' as later arrivals, with usable seismograms giving branch 'b' as the first arrival, was difficult. The most suitable event for this purpose is event 28 of Table 1, in which branch 'b' was the first arrival at all stations. The chosen event often showed a weak *P* arrival followed by a stronger *P* arrival about 2 seconds later. This phenomenon is well illustrated by the BATS seismograms in the left section of Fig. 3, where very small, but distinct early arrivals can be identified at stations YHNB and TDCB (too small to be seen with the scaling of the plot), but not at KMNB or NACB, where the earliest detectable arrival is strong. The earliest detectable energy arriving at NACB is also very late, forming an outlier in the data. The time picks generally lie close to the branch 'b', although the scatter is somewhat larger than for most other events used in deriving the models. Second arrivals that may be associated with branches 'a' and 'c' are visible at stations TWKB and MATB, respectively, with an additional strong arrival at WFSB lying close to the linear extension of branch 'a'. Later phases at the other broad-band stations are not clearly identifiable.

Because they are difficult to observe on single seismograms, the later arrival branches associated with triplications caused by discontinuities at transition zone depths have been previously identified by stacking seismograms at dense arrays of seismometers (Simpson *et al*., 1974; Ram and Mereu, 1977) or non-linear stacking at a more sparsely distributed network of stations (Simon *et al*., 2002). Following Simon *et al*. (2002), the phase-weighted stack (Schimmel and Paulsen, 1997) was used to demonstrate the presence of later arrival branches. Effective use of the method, however, requires careful selection and preparation of the data as explained below.

Arrivals from CWB stations from event 28 of Table 1 were not used in deriving the models WPSP01 and WPSP02 to minimize possible systematic bias due to model-dependent depth corrections. Events at depths greater than 100 km were used to define branches 'a' and 'b' (Table 1), but only to the extent that they were necessary to stabilize the inversion to estimate 'event bias corrections'. Processing of the present data to find later arrivals therefore provides an independent test of the reliability of the derived models. 11 of the 44 clear seismograms of event 28 recorded at the CWB network were chosen for phase-weighted stacking based on signal clarity, clustering of stations in central and southern Taiwan, and confinement

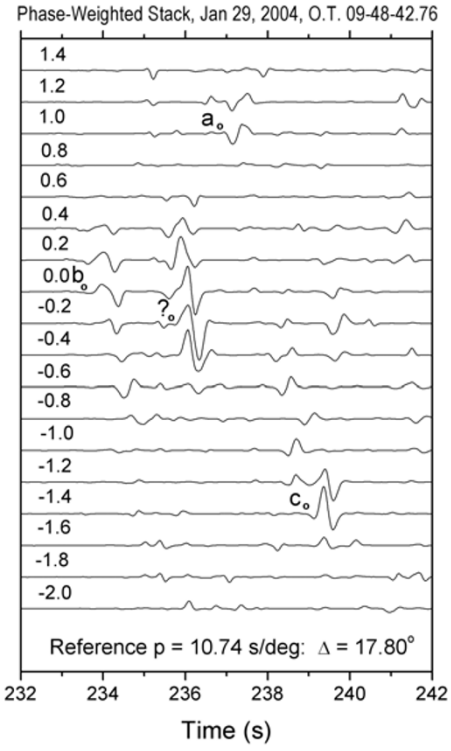

Fig. 8. Set of phase-weighted stacks at slownesses between −2.0 and 1.4 s/deg relative to the slowness of the first arrival branch 'b', produced from 11 CWB stations aligned with the *P* onset for station STY to provide a reference distance of 17.80°. The small circles define the onset times of signals attributed to branches 'a', 'b' and 'c', and an additional signal '?' 2.1 seconds after the *P* onset.

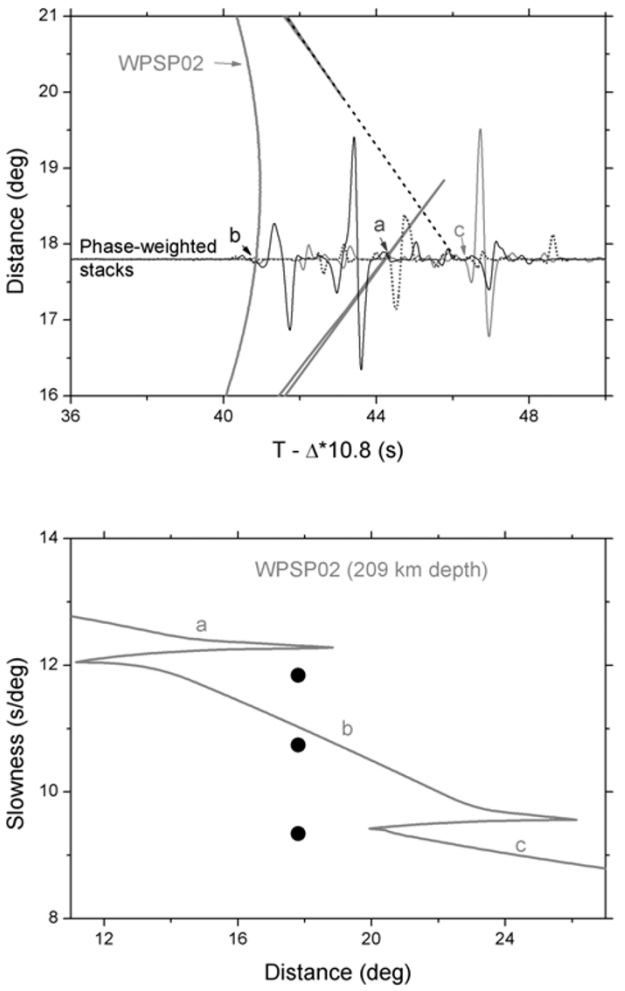

Fig. 9. (Top) The *P* travel-time curve computed from model WPSP02 for an event at a depth of 209 km, after applying a 'baseline' shift of 0.92 s to be consistent with Fig. 3, with three phase-weighted stacks plotted on top of each other at the reference distance of 17.80°. Black, dotted and grey lines correspond to the relative slownesses in Fig. 8 of 0.0, 1.0 and −1.4 s/deg, respectively. The dashed line is the linear extension of branch 'c' to a distance of 17.80°. (Bottom) Slowness curve computed by ray tracing through model WPSP02 for an event at 209 km depth. The dots are the slownesses of the maximum amplitudes of the three signals labelled 'b', 'a' and 'c' in the upper part of the figure.

to a distance range of less than 1.3° (17.21°–18.46°). These seismograms all showed a small *P* arrival followed by a stronger signal about 2 seconds later. 10 of them are plotted on the right side of Fig. 3 after application of station corrections; the seismogram from CHN4 (distance 18.03°) was not plotted because no station correction was available. Later arrivals close to the times expected from branch 'a' are clear only at ECL and TYC.

Before applying phase-weighted stacking, the seismograms were shifted in time to have the same arrival time as the reference station STY (distance 17.80°). The first four seconds following each *P* arrival were then cross-correlated with the first four seconds of two of the clearer seismograms (STY and ALS) to define small adjustments to the times of the seismograms that should result in better alignment of later arrivals. The amplitudes of the seismograms were also adjusted to have the same maximum peak-to-trough values over the same four-second period. Phase-weighted stacking was then undertaken using a phase weighting index of 3, and a smoothing window of 41 samples (0.4 s), at slowness intervals of 0.2 s/deg relative to the aligned traces over the range −2.0 to 1.4 s/deg. The slowness of branch 'b' at a distance of 17.80° is 11.03 s/deg for model WPSP02, while the slowness estimated from a quadratic polynomial fit to arrival times was 10.74 ± 0.10 s/deg. The difference between the predicted and measured slownesses is largely due to the uneven distribution and small number of stations (Fig. 3).

Figure 8 shows the phase-weighted stacks plotted as a function of travel time. At zero relative slowness, the earliest *P* arrival energy of branch 'b' arrives at a time of 233.5 s, followed by a stronger arrival about 2 s later, with a maximum amplitude at a slowness 0.2 s/deg lower. There is a signal arriving 3.4 s after the *P* onset at a relative slowness of 1.0–1.2 s/deg, which is attributed to branch 'a'. Then, 5.5 s after *P*, a strong signal arrives at a relative slowness of −1.4 s/deg, which can be associated with branch 'c'. The next step is to determine how well the slownesses and times of these arrivals agree with the predictions of one of the derived models, WPSP02.

The top half of Fig. 9 shows the phase-weighted stacks at relative slownesses of 0.0, 1.0 and −1.4 s/deg, plotted together at a distance of 17.80°. The travel-time curve calculated from model WPSP02 for an earthquake at a depth of 209 km is also plotted over the distance range 16°–21°, and the arrival time of the earliest *P* arrival has been adjusted to

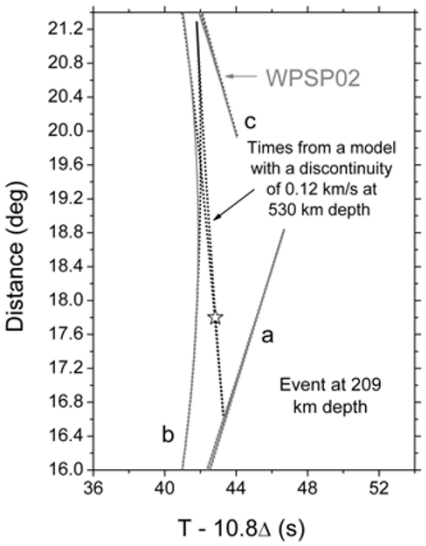

Fig. 10. Reduced travel-time curves from model WPSP02 (grey lines) and a model like WPSP02, but with an additional discontinuity of 0.12 km/s at a depth of 530 km (dotted lines). Travel-time branches are as in the caption to Fig. 5. The star marks the arrival at a distance of 17.8° attributed to the additional phase shown in Figs. 8 and 9.

fit branch 'b'. The trace for a relative slowness of 1.0 s/deg shows an arrival close to the expected time for branch 'a'. Over the distance range of the stack, the signal should consist of interfering refracted and reflected branches whose separations will differ from one input trace to another. The stacked output may therefore be influenced by phase shifts between input signals due to both this interference effect and differences in the curvature of branches 'a' and 'b'. Obvious similarity in the stacked outputs from branches 'a' and 'b' cannot therefore be expected. Although, on ray theory, branch 'c' terminates at 19.8°, wave theory predicts arrivals at shorter distances. A strong arrival is observed close to the linear extension of branch 'c' to 17.80° (dotted line), consistent with this idea.

The lower part of Fig. 9 shows the slowness–distance relation for an event at a depth of 209 km depth computed for model WPSP02. The slowness estimates for the arrivals marked 'a', 'b' and 'c' in the top half of Fig. 9 are plotted at a distance of 17.80°, and show reasonable agreement with the slownesses predicted at that distance by the model. Phase-weighted stacking has therefore identified two later arrivals that agree satisfactorily in both arrival time and slowness with the predictions from model WPSP02.

A possible explanation for the signal marked by a question mark in Fig. 8 is shown in Fig. 10. The travel-time curve calculated from model WPSP02 is plotted as the continuous grey line, as in Fig. 3. The travel times shown as dotted lines were calculated from a perturbed version of WPSP02. This perturbed model has a discontinuity of 0.12 km/s at a depth of 530 km, in which the wavespeeds were gradually decreased below a depth of 450 km to a value 0.07 km/s less than WPSP02 at 530 km depth. The increased wavespeeds at the discontinuity were tapered to fit on to WPSP02 at 610 km depth. The new model introduces an additional triplication with an arrival 1.1 s later and a slowness 0.6 s/deg lower than branch 'b' at a distance of 17.8°, which is marked by a star. In Fig. 8, the earliest energy of the large arrival marked by a question mark is about 1.6 s after branch 'b' (the small pulse before the circle at the onset of the large wavelet), and has a slowness 0.2 s/deg less than that of branch 'b'. Allowing for the uncertainties in the slownesses estimated by phase-weighted stacking, the agreement between the theoretical and estimated slownesses is fair, while the observed arrival is late by at least 0.5 s. The time separation between branch 'b' and the strong arrival can be increased by making the discontinuity larger or increasing its depth. However, in both cases the difference in slowness would become larger, while the existence of an additional discontinuity within the transition zone that is as prominent as either the 410- or 660-km discontinuity is not easy to explain.

A relatively small 520-km discontinuity has been reported in some regions, mostly from long-period observations (Shearer, 1990; Revenaugh and Jordan, 1991; Flanagan and Shearer, 1998). It has usually been attributed to the transformation of the β form of olivine to the spinel (γ) structure (Sinogeikin *et al*., 2003). However, litte or no evidence for the presence of this discontinuity has come from short-period P waves (Cummins *et al*., 1992; Vidale and Benz, 1992). The absence of frequent identifications of the 520-km discontinuity suggests a transition zone with a relatively low olivine content if the $\beta - \gamma$ transition is the cause. However, in instances when subducting slabs flatten above the 660-km discontinuity, a discontinuity near 520 km depth may be caused by majorite garnet above the γ form of olivine (Sinogeikin *et al*., 2003), giving rise to large P and S wavespeed increases of up to 6 and 9% respectively. Furthermore, the wavespeed gradients in the overlying region around the contact between former basaltic crust and average mantle would be low or possibly negative. This phenomenon would also explain the low amplitude of the 'b' branch in Fig. 8. The additional phase may therefore be caused by another discontinuity near 530 km depth, localized in the vicinity of a sub-horizontal slab, but more data, allowance for the effects of lateral heterogeneity, waveform modelling, and further work on resolving the complicated plate geometry of the region (Wright, 2007), will be required to fully explain its late arrival time and large amplitude.

7. Model Uncertainties

The uncertainties in one-dimensional earth models derived by inversion of body waves have often been determined (Wiggins *et al*, 1973; Walck, 1984), but by methods that are non-probabilistic in the sense that increasing the number of observations does not reduce the uncertainties. A probabilistic approach to analyzing uncertainties in P wavespeed models was discussed by Simon *et al*. (2002) using data and analysis methods similar to those of the present paper. A modified approach to the error evaluation is presented here to quantify the contributions due to errors in travel-time branches that are later arrivals but not observed directly. Smooth wavespeed models were constructed through fitting low-degree polynomials through the travel-time branches (Table 3), which allow error estimates to be made for the distance ranges where travel-time

branches are second arrivals.

The errors in fitting a polynomial through a set of travel times are minimum at the centroid of the data points, and can be estimated at any distance through use of a simple formula. In contrast, errors in summary value curve fitting (Bolt, 1978), which was used by Simon *et al*. (2002), can only be made at discrete points within the distance range of the observations. The errors in summary value curve fitting are generally larger at a particular distance than those determined from polynomial fitting, due to the smaller range of distances employed. This effect is simply the usual trade-off procedure between 'window length' and variance, originally discussed by Backus and Gilbert (1970), and, for seismic wavespeed estimates, by Wright (2006). Errors in wavespeeds were therefore estimated from the slowness curves produced by both polynomial regression and summary value smoothing, and the larger value at any depth was chosen as the preferred error.

Fig. 6 (right) shows model WPSP01 with 95 % confidence limits (2 × standard errors). The confidence limits for the upper mantle start at 0.33 km/s where the inversion begins at 110 km depth, and decrease to a minimum of 0.17 km/s at 175 km depth. There is then a gradual increase in the confidence limits to about 0.35 km/s at a depth of 270 km. From 270 km to the discontinuity at 325 km depth, the errors decrease a little, but are not accurately defined, because of the absence of well-constrained estimates of errors in slowness on branch 'a' as a second arrival; these errors were calculated from the formula for the error in the first derivative of the polynomial representation of branch 'a'. The wavespeeds in the transition zone correspond to a depth range from 325 to 676 km (351 km) with 95% confidence limits ranging between 0.20 and 0.39 km/s over the depth range 361 km to 608 km for which branch 'b' is the first arrival, with the minimum at a depth of 470 km. Errors in the *P* avespeeds in the lower mantle are fairly low where branch 'c' becomes the first arrival (706 km depth), lying in the range 0.21 km/s to 0.38 km/s between 706 and 760 km. At greater depths the errors increase rapidly due to the relatively small amount of data.

Error estimates on the depths of the discontinuities were derived by evaluating the Herglotz-Wiechert integral along alternative paths defined by the slowness values with the standard error added or subtracted. The depths obtained from the integration depend largely on the shapes of the slowness curves, so that the errors can be quite small, even when there are reasonably large errors in slowness. Very smooth slowness curves, like the ones used to derive models WPSP01 and WPSP02, will yield smaller depth errors than ones that contain short-wavelength variations, because of the usual trade-off relationships discussed by Backus and Gilbert (1970). These errors for the depths of the discontinuities at 325 km and 676 km were 1.5 and 1.6 km respectively, which are minimum values for an average smooth model for the region sampled. However, deviations from spherical symmetry and errors in the distances and focal depths of the earthquakes used, provide additional uncertainties that are estimated to give total errors of about 6 and 7 km for the average depths of the upper and lower discontinuities, respectively.

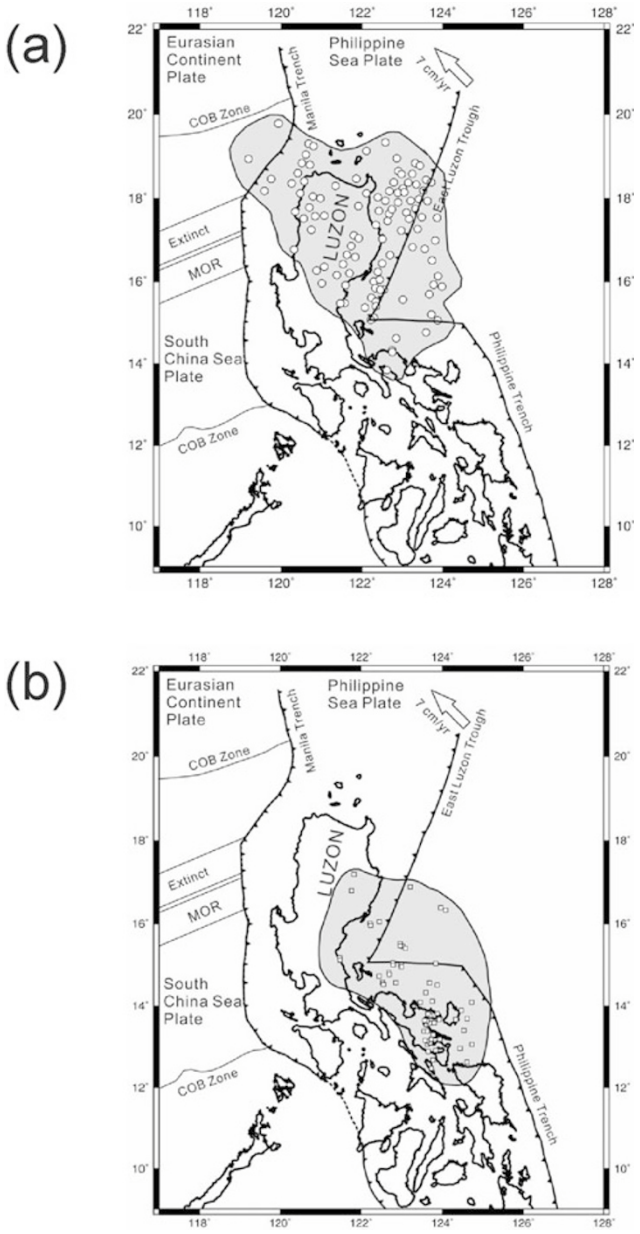

Fig. 11. Plate boundaries for the region from Taiwan to the southern Philippines, with highlighting of regions of upper mantle (a) and topmost transition zone (b) covered by the present data. Circles in (a) and squares in (b) denote the mid-points of the ray paths between the stations and the event locations corrected back to their surface-focus equivalents.

8. Mantle Structure

8.1 Properties and locality of wavespeed model

The region of the upper mantle covered by the first arrival data for branch 'a' (depth range 110–290 km) incorporates the region south of 20°N between the Manila trench and the East Luzon trough, and south of 19°N, east of the East Luzon trough (Fig. 11(a)). The region extends south to about 14°N west of the Philippine trench, and encircles most of the northern part of the island of Luzon. The upper mantle wavespeeds to 290 km depth are lower than those of IASP91 (Fig. 12), as expected for an oceanic region of the upper mantle. The arrival times are frequency-dependent with shorter times for longer periods, which is consistent with the presence of a poorly-defined low wavespeed zone

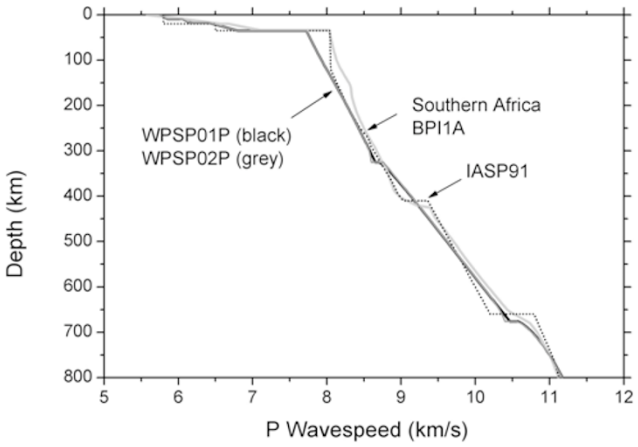

Fig. 12. *P* models BPI1A (light grey) (Simon *et al*. 2002), IASP91 (dotted line) (Kennett, 1991), WPSP01P (black) and WPSP02P (grey).

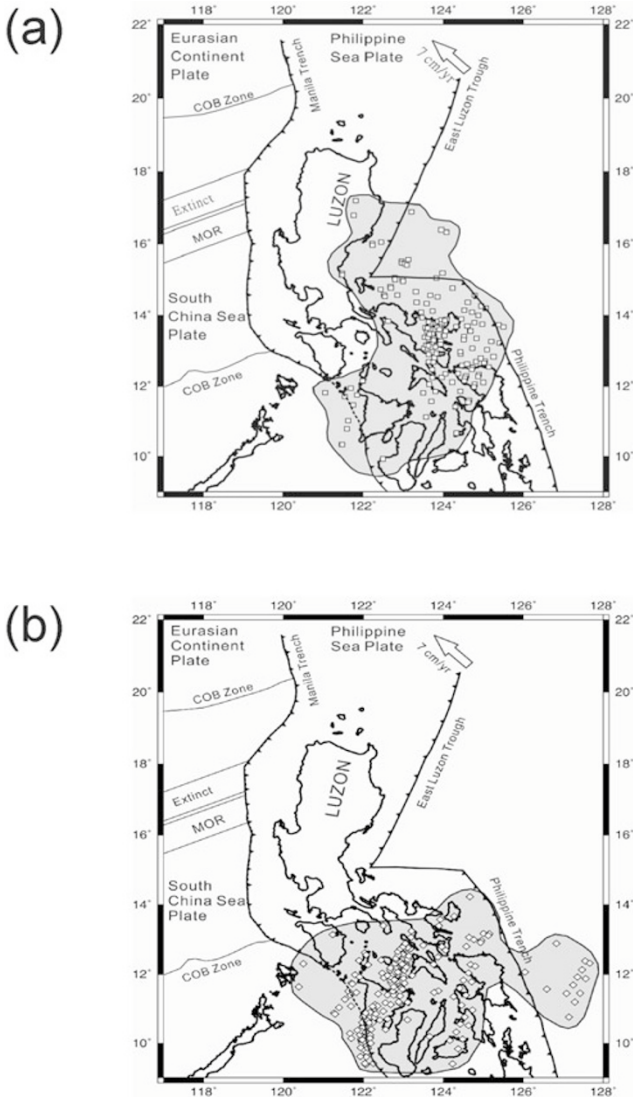

Fig. 13. Plate boundaries for the region from Taiwan to the southern Philippines, with highlighting of regions of the transition zone (a) and lower mantle (b) covered by the present data. Squares in (a) and diamonds in (b) denote the mid-points of the ray paths between the stations and the event locations corrected back to their surface-focus equivalents.

in the upper mantle at depths above 200 km, similar to that reported by Nowack *et al*. (1999). The smoothest possible curve that will allow a Herglotz-Wiechert inversion has been fitted through the travel times, which show much more scatter than for times of arrivals that have penetrated to transition zone and lower mantle depths.

The region of the transition zone covered by signals that are first arrivals between distances of 17.7° and 21.0°, or the topmost part of the transition zone between depths of 360 km and 480 km, is shown in Fig. 11(b). It is well to the east of the Manila trench, and comprises eastern Luzon and the area to the east on both sides of the East Luzon trough, and south to the area of the Philippine trench just north of 12° N. This part of the mantle appears to have the 410 km discontinuity elevated to a depth of only 325 km. The data for branch 'b' show limited scatter (standard deviation on polynomial fit of only 0.86 s), suggesting that the elevated discontinuity is not a localized phenomenon in a descending slab, but is probably spread over a broader region. The presence of a trapped, almost horizontal, and cool subducted slab at depths below 300 km, was suggested by Wright (2007), who proposed a plate tectonic model based on the work of Yang *et al*. (1996) and Bautista *et al*. (2001).

If we consider the entire transition zone, the region covered extends further south to about 10°N (Fig. 13(a)), though the coverage is strongly weighted by the paths in the eastern region closer to the Philippine trench beneath southern Luzon and the islands to the south (Masbate and Samar). The region of the uppermost lower mantle mapped by the data encompasses the southern part of Luzon and adjacent islands, and east and south of this area to the east of the Philippine trench (Fig. 13(b)). The region extends southwards to about 9°N. The densest area of coverage lies well to the south of the southern tip of the Manila trench and forms a north-south trending band between 122° and 123° E at latitudes 12° to 9°N.

8.2 Comparison with similar studies in other regions

An important consideration is the accuracy with which the depth to the 410 km discontinuity is determined. Some of the old studies of the transition zone using refracted *P* waves provide estimates of the depth of the 410 km discontinuity that are closer to that of the present study than those from converted waves. For example, Niazi and Anderson (1965) estimated a depth of only 320 km for the 410 discontinuity beneath western North America, whilst Simpson *et al*. (1974) had a region of increased wavespeed gradients above 400 km depth below northeastern Australia. Both of these investigations relied on slowness measurements for many earthquakes at arrays of seismometers with apertures of 25 km or less. Unlike the present work, neither study provides a clear definition of the travel-time gradients of branches 'a', 'b' and 'c' over a long distance range. The estimates of the depths to both discontinuities in these studies are therefore less reliable than in the present work.

The critical evidence for defining the depth to the '410 km discontinuity' is the accurate location of branch 'b' (Fig. 5). A more rapid change in slope of the travel-time curve near 17.7° distance (Fig. 5) can be inferred from

the data (see Section 9), and the greatest uncertainty is in defining branch 'a'. Figure 12 shows models WPSP01P and WPSP02P, model BPI1A (Simon *et al*., 2002), chosen because it was derived by a similar methodology, including the use of 'event bias corrections', and reference model IASP91 (Kennett, 1991). Models WPSP01P and WPSP02P lie close to the IASP91 model below depths of 150 km and have slightly lower wavespeeds below 250 km depth. The need to have a shallow discontinuity at 325 km depth is therefore not due to any unusual properties of the region above, which is reasonably typical of oceanic upper mantle. Beyond the cross-over point at a distance of 17.7°, the *P* arrival of branch 'b' (Fig. 5) has penetrated to depths of 360 km and greater. If the depth of the inferred discontinuity is increased, branch 'b' becomes systematically late with respect to the observed data, with an observable misfit for an increase of only 2 km. The data for branch 'b' therefore require that any model has higher wavespeeds than IASP91 or a continental model like BPI1A at depths between 325 and 410–420 km.

Very few investigations have attempted to accurately measure the wavespeed gradients in the transition zone through definition of the slope of branch 'b' where it is the first arrival. Exceptions are the studies of Zhao *et al*. (1999) and Simon *et al*. (2002), which give comparatively large wavespeed gradients within the transition zone, implying smaller jumps in wavespeed across the 410 and 660 km discontinuities than in many other studies using refracted *P* arrivals. The high wavespeed gradients in the transition zone in the present models suggest a small jump in wavespeed across the discontinuity at 325 km depth, because of the increased thickness (351 km) compared with other models of the transition zone. Li *et al*. (2000) found a gap in *P*-to-*SV* conversions at latitudes close to 135°E in the Japan subduction zone where the slab penetrates below 400 km depth. Perhaps the changes in elastic parameters that occur for an elevated discontinuity are too small to provide observable converted *S* waves, requiring alternative methods for its detection.

Another consequence of the high wavespeed gradients in the transition zone is that the agreement with wavespeed models constructed from experimental petrology and mineral physics is poorer than in many other models derived from seismological observations (Fujisawa, 1998; Nishihara and Takahashi, 2001). The present models WPSP01 and WPSP02 yield a dV_p/dz value of 4.8 $\times 10^{-3}$ s^{-1} for the depth range 400–600 km, compared with 4.3x10^{-3} s^{-1} for a komatiite (piclogite) model and 2.7$\times 10^{-3}$ s^{-1} for a pyrolite model (Nishihara and Takahashi, 2001). Nishihara and Takahasi give a range of (2.1–5.1)$\times 10^{-3}$ s^{-1} for this gradient, so that the present models yield wavespeed gradients close to their upper bound, and closer to the predicted gradients of the komatiite model than the pyrolite model. The presence of water in the transition zone and the comparison of seismically-derived wavespeeds with experimentally-determined values for dry conditions may also provide an explanation of part of the observed discrepancies. Clearly more studies that attempt to directly measure the wavespeed gradients within the transition zone are required.

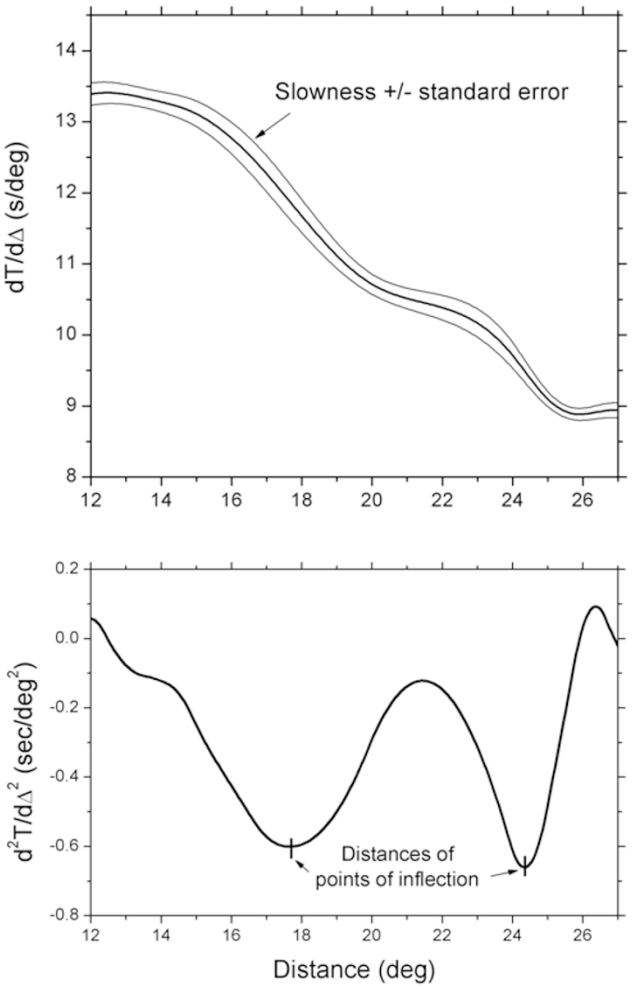

Fig. 14. Results of numerical differentiation of the first arrival times.

Estimates of the thickness of the transition zone have usually been made from *P*-to-*SV* or *SV*-to-*P* converted waves (e.g. Li *et al*., 2000), *ScS* reverberations (Revenaugh and Jordan, 1991) or precursors to long-period *PP* and *SS* phases (Shearer and Flanagan, 1999), so that the thickness is defined as the separation of the regions of highest wavespeed gradients or wavespeed discontinuities that give rise to mode conversions or reflections. However, such an approach may fail to provide meaningful estimates of transition zone thicknesses in regions where the 410 kilometre discontinuity is elevated and has small wavespeed contrasts.

9. Discussion

Nowack *et al*. (1999) used extensive CWB data for approximately the same region as the present study, and had a 410 km discontinuity at a more usual depth of 406 km. We agree with Nowack *et al*. that there is a high wavespeed anomaly in the mantle below the western margin of the Philippine Sea plate at depths somewhere between 300 and 500 km. They propose high wavespeeds in the uppermost part of the transition zone below 406 km depth, whereas the present work suggests that the high wavespeeds start at much shallower depths as an elevated 410 km discontinuity in a cold sub-horizontal subducted plate (Wright, 2007). The crucial evidence is observations of branch 'b' of

the travel-time curve (Fig. 5), whose presence can be confirmed objectively by numerical differentiation of the corrected first arrival times using summary value smoothing (Bolt, 1978) followed by cubic spline interpolation. Figure 14 shows a slowness-distance relationship constructed with the short-wavelength perturbations smoothed out. The important feature is the rapid decrease in slowness at distances beyond 17.0°, confirming that the high-wavespeed anomaly starts at relatively shallow depths, and providing the basis for the additional analysis that led to the identification of the cross-over distance between branches 'a' and 'b' at 17.7°. In the lower part of Fig. 14, $d^2T/d\Delta^2$ plotted as a function of distance shows the two clear minima that define the points of inflection of the slowness curve close to the inferred cross-over distances at 17.7° (a-b) and 24.2° (b-c). A comparison of the travel-time curves calculated from Nowack *et al.*'s model TS.406 with those from WPSP02P is provided in Appendix B to show the extent of the misfit of the model TS.406 times to the present data.

An important consideration is the use of relatively deep events and possible effects on the derived models. The main factor that determines how the focal depth contributes to the uncertainties in correcting times to their equivalent surface-to-surface distances is the ratio of the depth of an event to the maximum depth of penetration of the seismic energy. Provided this ratio is small, the effect is negligible, even if the model used to derive the corrections is only an approximate representation of the structure between the focus and the surface. In the present work, the distance correction is most important, since any effects of incorrect time shifts are largely eliminated in constructing the corrected travel times. The choice of a reference model used to compute the corrections has the effect of biasing the final model slightly towards the reference model, the amount depending in a complicated manner on both the depth distribution of the events used and how the differences between the reference model and the real earth are distributed in depth. To provide constraints on the possible effects of errors that could have been introduced by choosing the IASP91 model to provide depth corrections, the depth and time corrections computed from model WPSP02 were compared with those from IASP91 for hypothetical earthquakes at depths of 100, 150, 200, 550 and 600 km. Distance-dependent differences in distance corrections between these models have the effect of pushing the slowness in that distance interval away from that of the real earth towards that predicted by the reference model.

The deepest event providing times for branch 'a' is at 71 km depth (Table 1, event 13). For an event at 100 km depth, the differences in distance corrections between WPSP02 and IASP91 (DWI) are distance-dependent and always negative (corrections smaller for WPSP02 than for IASP91), with a maximum magnitude of 0.3°. The DWI values will be smaller for an event at 71 km depth, so that the errors in depth corrections have no significant influence on the definition of branch 'a'. The next consideration is the effect of depth corrections on the distance of the cross-over between branches 'a' and 'b'. All events that have stations straddling the cross-over (events 2, 3, 5 and 29 of Table 1) have focal depths of 31 km or less, so that the depth corrections do not affect this distance, provided the branches have been correctly identified. For branch 'b', six events at depths greater than 100 km were used to obtain a sufficiently dense distance coverage to make the method of deriving 'event bias corrections' effective. One of these events has a station close to the cross-over (event 1 of Table 1), while the remaining 5 have corrected distances at least 1.3° greater than the cross-over distance. Event 28 (Table 1) is the deepest event at 209 km depth. Events at 100, 150 and 200 km depth have DWI values of 0.13°, 0.22° and 0.34° at the cross-over between branch 'a' and 'b', and −0.10°, −0.16° and −0.22°, respectively, at the cross-over between branches 'b' and 'c'. These differences arise from the higher wavespeed gradients of model WPSP02 than IASP91 in the transition zone. The adverse effect of using IASP91 to calculate distance corrections is therefore small, imposing slightly lower wavespeed gradients in the transition zone than if a model like WPSP02 had been used. Moreover, if the model of Nowack *et al.* (1999), with its lower wavespeed gradients in the transition zone, had been used to compute distance corrections, they would not have differed significantly from those used.

Two of the events at depths between 120 and 200 km (events 9 and 11 of Table 1) and seven shallower events straddle the cross-over point between branches 'b' and 'c'. DWI values for branch 'c' are much smaller than for branch 'b', and any influence of corrections for focal depth on the cross-over distance is negligible. The three events at depths greater than 550 km (events 4, 15 and 17 of Table 1) were selected because of their clear onsets and the possibility that they would provide information on both branches 'b' and 'c'. However, all three events gave first arrivals that belong to branch 'c', so that possible errors in corrected distance have no effect on branch 'b'. The DWI value for an event at 550 km depth has its largest magnitude (−0.3°) at the minimum distance of (15.0°), which is close to the minimum distance of observations for event 15 (Table 1). Events at depths of 550 and 600 km provide DWI values of zero and less than 0.1° at the corrected distance of the cross-over, respectively, and slightly greater than 0.2° for both depths at the maximum distance of observation. Thus, the distance corrections do not have significant uncertainties for the deep events, mainly because the structure in the uppermost lower mantle differs little from that of the IASP91 model.

10. Conclusions

A *P* wave profile constructed using earthquakes south of Taiwan as sources recorded by stations in and around Taiwan showed the following characteristics for the mantle below and around Luzon:

(a) The upper mantle has seismic wavespeeds typical of oceanic mantle, and a weakly-defined low wavespeed zone above 200 km depth whose properties are poorly defined.

(b) The 410-kilometre discontinuity is elevated to about 325 km depth in a region of complex subduction, suggesting anomalously low temperatures in the lowermost upper mantle and uppermost transition zone. Identification of a rapid decrease in slowness of the earliest *P* arrivals at distances around 17.7° was the critical evidence that supported the concept of an elevated discontinuity to explain the in-

ferred travel-time anomaly for the region, rather than the high wavespeeds in the transition zone below 406 km depth proposed by Nowack *et al*. (1999).

(c) A thick transition zone has both high wavespeed gradients and low wavespeed contrasts across the discontinuities that define its upper and lower boundaries compared with many other seismologically-derived models. Evidence for a 520-kilometre discontinuity was not definitive, although phase-weighted stacking demonstrated the presence of an additional strong later arrival phase that may be caused by a localized discontinuity near 530 km depth.

(d) The 660-kilometre discontinuity is slightly depressed with respect to the global average, at a depth of 676 km. Errors in the average depths of the upper and lower discontinuities are about 6 and 7 km, respectively.

The presence of the later travel-time branches at the appropriate times to be produced by an elevated discontinuity at 325 km and the discontinuity at 676 km depth was confirmed by phase-weighted stacking of a cluster of 11 short-period seismograms from the CWB network, thereby showing that the cross-over distance between branches 'a' and 'b' was accurately located.

Acknowledgments. This research was funded by the Science Council of Taiwan. C. Wright also thanks the Science Council of Taiwan and the Institute of Earth Sciences, Academia Sinica, for support as part of a visiting scholar programme. The assistance of Shiue-Mei Huang, Wen-Tzong Liang, Zaw Min Maung and Jin Tsai Su with the preparation and analysis of the data is gratefully acknowledged. The authors also thank Kazuaki Omamoto for providing insights into problems of reconciling mantle petrology with seismological data. Figs. 1, 2, 11 and 13 were produced with the assistance of Generic Mapping Tools (Wessel and Smith, 1995).

Appendix A.

The correct location of the cross-over distances between branches 'a' and 'b' and 'b' and 'c' requires careful analysis, because of the relatively small changes in slowness at the cross-over points compared with similar data from some other regions of the Earth. Because of the unusually shallow depth of the 410 km discontinuity, the process of locating the cross-over distance between branches 'a' and 'b' is described in detail. The preferred location at a distance of 17.7° was also checked by numerical differentiation of the first arrival times (Fig. 14).

The best quality data for determining the slopes of branches 'a' and 'b' come from relatively deep events. Such events have either all or just one or two stations on one side of the cross-over distance, so that the slownesses of branches 'a' and 'b' are relatively easy to define. The events that straddle the cross-over are relatively shallow (events 2, 3, 5 and 29 of Table 1), and the emergent onsets of the *P* phase are less clear than for the deeper events. The location of the cross-over cannot be reliably determined by visual inspection of the seismograms or measured times for an individual event, because of the small number of stations and their uneven distribution with respect to distance. Moreover, the process of correcting times for focal depth has to be done by trial and error to make sure that the corrections are made for the correct branch. Computations were therefore undertaken for a range of possible cross-over points, and a preferred solution chosen.

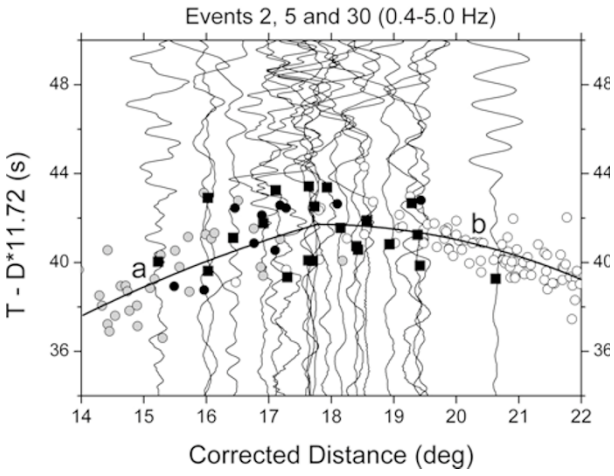

Fig. A.1. Seismograms from selected stations for shallow earthquakes 2, 5 and 30 of Table 1, whose corrected distances straddle the cross-over distance (17.7°) between travel-time branches 'a' and 'b'. Squares and black circles, respectively, mark the *P* onset times of the plotted seismograms and those from events 2, 5 and 30 that have been omitted. The grey and open circles denote the onset times of the events whose stations lie on the low and high distance sides of the cross-over, respectively. 'Event bias corrections' and corrections for focal depth were applied to all data.

In the present work a distance of 17.7° is the preferred cross-over distance. The resulting travel-time curves are shown in Fig. A1 in which only the first arrival segments of branches 'a' and 'b' are plotted. The reduced time scale has been chosen so that the reducing slowness (11.72 s/deg) is the same as that of branch 'b' at a distance of 17.7°; branch 'b' therefore has zero gradient at this distance. Only 21 of the 31 seismograms of shallow events 2, 3 and 5 of Table 1 are plotted; 10 were omitted to avoid cluttering the figure with traces that were too closely spaced. Trace amplitudes were normalized to give the same peak-to-peak maximum value for all stations of a particular event, and to give comparable noise levels for different events. Station and 'event bias corrections' were applied to all seismograms and plotted times, and the symbols used for the times are explained in the caption for Fig. A.1.

The reliable picking of the times of the earliest *P* arrivals for BATS stations for shallow events is not a simple procedure, and it is very easy to pick systematically late. The picking is more difficult for CWB stations, and no CWB data for branch 'a' were used in the present work. The data discussed in the next section (Fig. B.1) suggests that the *P* arrivals for branch 'a' from shallow events recorded at CWB stations may have been picked late in the data of Nowack *et al*. (1999). This would explain their lower upper mantle wavespeeds, which are only partly accounted for by the application of 'event bias corrections' in the present work.

Appendix B.

The earlier work of Nowack *et al*. (1999) for this region identified a time anomaly in the upper transition zone, with a 410-km discontinuity at a normal depth. It is therefore important to explain why the depth of the discontinuity differs so much from their interpretation based on data that covered

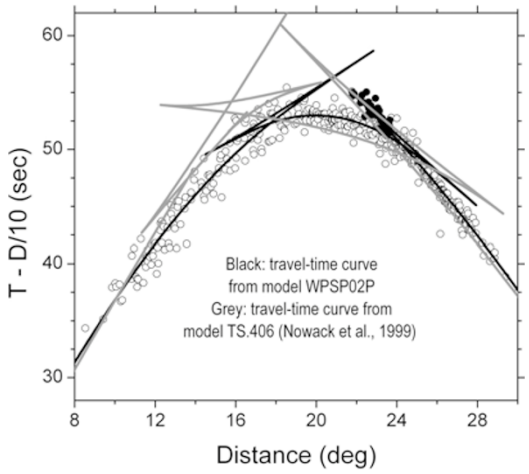

Fig. B.1. Corrected time data from the lower half of Fig. 5, with travel-time curves of models WPSP02P and TS.406 of Nowack *et al.* (1999). The triplication and shadow zone with a cross-over distance close to 13.6° are caused by the small low wavespeed zone in model TS.406.

a similar region to that of the present study. The critical evidence for defining the depth to the 410 km discontinuity is the accurate location of refracted arrival energy from within the transition zone. Figure B.1 shows the travel-time curves computed from models TS.406 of Nowack *et al.* (1999) and WPSP02, superimposed on the corrected times of Fig. 5 (bottom section). There is agreement between the two models at the shortest and largest distances, with major discrepancies in between. The most striking discrepancy is the absence of curvature and the shift in position of branch 'b' from model TS.406 to earlier times relative to the present data. A major contribution to the difference in Nowack *et al.*'s interpretation is the failure of their data to accurately resolve the position and gradient of the refracted arrival branch through the transition zone. There are, however, other factors that are discussed below.

Nowack *et al.* (1999) computed station corrections from their average travel-time curve. In the present work, the station corrections were computed using only those *P* arrivals that had penetrated to lower mantle depths and the *ScP* phase, which results in more stable station corrections with lower standard errors, as discussed in Section 3.2. However, a major difference in the present analysis from that of Nowack *et al.* and other similar studies (e.g. Zhao *et al.*, 1999) is the application of 'event bias corrections'. These corrections lie is in the range −2.6 to 1.3 s, giving a range of about 4 s; the estimated standard errors lie in the range 0.07 to 0.21 s, with the larger values near the high and low distance limits of the data. The large range of these corrections shows that the spurious discontinuities in time may be introduced in this type of study when combining times from several events and stresses the need to remove them. The dominant cause is errors in origin times in the hypocentral information provided in earthquake bulletins. In addition, the 'event bias corrections' compensate to some extent for the low seismic wavespeeds at shallow depths in the mantle that are present in the Philippines and Indonesian regions.

The scatter of 'event bias corrections' over a range of about 4 seconds is not a phenomenon restricted to the western part of the Philippine Sea plate and adjacent regions of complex subduction. A similar range of corrections was found by Simon *et al.* (2002) for shallow earthquakes within and around southern Africa. We therefore suggest that 'event bias corrections' should be routinely made for most studies of the upper mantle and transition zone that use refracted body waves, which will assist in both maximizing resolution of structure and in suppressing the effects of lateral heterogeneities in the earthquake source regions. Kagan (2003) reported that the errors in origin times (standard deviation, σ) of events listed in PDE or ISC catalogues were on average about one second. Thus, if it were possible to determine the errors in origin times for a small number of earthquakes selected randomly from a particular region, a spread of about $\pm 2\sigma$ or 4 seconds would be expected. This is very close to the observed range of 'event-bias corrections', which are rough estimates of origin time errors contaminated by the errors in correcting times to their surface-focus equivalents.

References

Anderson, D. L. and J. D. Bass, Mineralogy and composition of the upper mantle, *Geophys. Res. Lett.*, **11**, 637–640, 1984.

Anderson, D. L. and M. N. Toksöz, Surface waves on a spherical earth, 1, upper mantle structure from Love waves, *J. Geophys. Res.*, **68**, 3483–3499, 1963.

Backus, G. E. and W. F. Gilbert, Uniqueness in the inversion of inaccurate gross earth data, *Philosophical Transactions of the Royal Society of London A*, **266**, 187–269, 1970.

Bass, J. D. and D. L. Anderson, Composition of the upper mantle: geophysical tests of two petrological models, *Geophys. Res. Lett.*, **11**, 237–240, 1984.

Bass, J. D. and F. Schilling, Editorial: Introduction to special issue on phase transitions and mantle discontinuities, *Phys. Earth Planet. Int.*, **136**, 1–2, 2003.

Bautista, B. C., M. L. P. Bautista, K. Oike, F. T. Wu, and R. S. Punongbayan, A new insight on the geometry of subducting slabs in northern Luzon, Philippines, *Tectonophysics*, **339**, 279–310, 2001.

Bolt, B. A., Summary value smoothing of physical time series with unequal intervals, *J. Comput. Phys.*, **29**, 357–369, 1978.

Chen, Y.-H., S. W. Roecker, and G. L. Kosarev, Elevation of the 410 km discontinuity beneath the central Tien Shan: Evidence for a detached lithosphere root, *Geophys. Res. Lett.*, **24**, 1531–1534, 1997.

Chen, P.-F., B.-S. Huang, and W.-T. Liang, Evidence of a slab-subducted lithosphere beneath central Taiwan from seismic waveforms and travel times, *Earth Planet. Sci. Lett.* **229**, 61–71, 2004.

Collier, J. D. and G. R. Hellfrich, Topography of the "410" and "660" km seismic discontinuities in the Izu-Bonin subduction zone, *Geophys. Res. Lett.*, **24**, 1535–1538, 1997.

Cummins, P. R., B. L. N. Kennett, J. R. Bowman, and M. G. Bostock, The 520 km discontinuity?, *Bull. Seism. Soc. Am.*, **82**, 232–236, 1992.

Duffy, T. S. and D. L. Anderson, Seismic velocities in mantle minerals and the mineralogy of the upper mantle, *J. Geophys. Res.*, **94**, 1895–1912, 1989.

Duffy, T. S., C.-S. Zha, R. T. Downs, H.-K. Mao, and R. J. Hemley, Elasticity of forsterite to 16 GPa and the composition of the upper mantle, *Nature*, **378**, 170–173, 1995.

Flanagan, M. P. and P. M. Shearer, Global mapping of topography on transition zone velocity discontinuities by stacking SS precursors, *J. Geophys. Res.*, **103**, 2673–2692, 1998.

Fujisawa, H., Elastic wave velocities of forsterite and its β-spinel form and chemical boundary hypothesis for the 410-km discontinuity, *J. Geophys. Res.*, **103**, 9591–9608, 1998.

Ibrahim, A. K. and O. W. Nuttli, Travel-time curves and upper mantle structure from long-period *S* waves, *Bull Seismol. Soc. Am.*, **57**, 1063–1092, 1967.

Ita, J. and L. Stixrude, Petrology, elasticity and composition of the mantle transition zone, *J. Geophys. Res.*, **97**, 6849–6866, 1992.

Kagan, Y., Accuracy of modern global earthquake catalogs, *Phys. Earth*

Planet. Int., **135**, 173–209, 2003.

Kaiho, K. and B. L. N. Kennett, Three-dimensional seismic structure beneath the Australian region from refracted wave observations, *Geophys. J. Int.*, **142**, 651–668, 2000.

Kato, M. and I. Nakanishi, Upper mantle velocity structure in the western Pacific rim estimated from short-period recordings at Matsushiro Seismic Array System, *Earth Planets Space*, **52**, 459–466, 2000.

Kennett, B. L. N. (Ed.), *IASPEI 1991 Seismological Tables*, 167 pp., Research School of Earth Sciences, Australian National University, Canberra, Australia, 1991.

Kim, K.-H., J.-M. Chiu, H. Kao, Q. Liu, and Y.-H. Yeh, A preliminary study of crustal structure in Taiwan region using receiver function analysis, *Geophys. J. Int.*, **159**, 146–164, 2004.

Li, B., R. C. Liebermann, and D. J. Weidner, Elastic moduli of wadsleyite (β-Mg_2SiO_4) to 7 gigapascals and 873 kelvin, *Science*, **281**, 675–677, 1998.

Li, X., S. V. Sobolev, R. Kind, X. Yuan, and C. Estabrook, A detailed receiver function image of the upper mantle discontinuities in the Japan subduction zone, *Earth Planet. Sci. Lett.*, **183**, 527–541, 2000.

Ma, K.-F., J.-H. Wang, and D. Zhao, Three-dimensional seismic velocity structure of the crust and uppermost mantle beneath Taiwan, *J. Phys. Earth*, **44**, 85–105, 1996.

Negredo, A. M., J. L. Valera, and E. Carminati, TEMSPOL: a MATLAB thermal model for deep subduction zones including major phase transformations, *Computers and Geosciences*, **30**, 249–258, 2004.

Niazi, M. and D. L. Anderson, Upper mantle structure of western North America from apparent velocities of *P* waves, *J. Geophys. Res.*, **70**, 4633–4640, 1965.

Nishihara, Y. and E. Takahashi, Phase relation and physical properties of Al-depleted komatiite to 23 GPa, *Earth Planet. Sci. Lett.*, **190**, 65–77, 2001.

Nowack, R. L., E. Ay, W.-P. Chen, and B.-S. Huang, A seismic profile of the upper mantle along the south western edge of the Philippine Sea plate using short-period array data, *Geophys, J. Int.*, **136**, 171–179, 1999.

Okamoto, K. and S. Maruyama, The eclogite-garnetite transformation in the MORB + H_2O system, *Phys. Earth Planet. Int.*, **146**, 283–296, 2004.

Ram, A. and R. F. Mereu, Lateral variations in upper mantle structure around India as obtained from Gauribidanur seismic array data, *Geophys. J. R. Astron. Soc.*, **49**, 87–113, 1977.

Revenaugh, J. S. and T. H. Jordan, Mantle layering from *ScS* reverberation, 2, The transition zone, *J Geophys. Res.*, **103**, 2673–2692, 1991.

Ringwood, A. E., A model for the upper mantle, *J. Geophys. Res.*, **67**, 857–867, 1962.

Ringwood, A. E., Phase transformations and their bearing on the constitution and dynamics of the mantle, *Geochimica et Cosmochimica Acta*, **55**, 2083–2110, 1991.

Schimmel, M. and H. Paulssen, Noise reduction and detection of weak, coherent signals though phase-weighted stacks, *Geophys. J. Int.*, **130**, 497–505, 1997.

Schmeling, H., R. Monz, and D. C. Rubie, The influence of olivine metastability on the dynamics of subduction, *Earth Planet. Sci. Lett.*, **165**, 55–66, 1999.

Shearer, P. M., Seismic imaging of upper mantle structure with new evidence for a 520-km discontinuity, *Nature*, **344**, 121–126, 1990.

Shearer, P., *Introduction to Seismology,* 260 pp., Cambridge University Press, Cambridge, U.K., 1999.

Shearer, P. M. and M. P. Flanagan, Seismic velocity and density jumps across the 410- and 660-kilometer discontinuities, *Science*, **285**, 1545–1548, 1999.

Simon, R. E., C. Wright, E. M. Kgaswane, and M. T. O. Kwadiba, The *P* wavespeed structure below and around the Kaapvaal craton to depths of 800 km, from traveltimes and waveforms of local and regional earthquakes and mining-induced tremors, *Geophys. J. Int.,* **151**, 132–145, 2002.

Simon, R. E., C. Wright, M. T. O. Kwadiba, and E. M. Kgaswane, Mantle structure and composition to 800-km depth beneath southern Africa and surrounding oceans from broadband body waves, *Lithos Special Issue: The Slave-Kaapvaal Workshop: A Tale of Two Cratons*, edited by A. G. Jones, R. W. Carlson, and H. Grutter, **71**, 353–367, 2003.

Simpson, D. W., R. F. Mereu, and D. W. King, An array study of *P* wave velocities in the upper mantle transition zone beneath northwestern Australia, *Bull. Seismol. Soc. Am.*, **64**, 1757–1788, 1974.

Sinogeikin, S. V., J. D. Bass, and T. Katsura, Single-crystal elasticity of ringwoodite to high pressures and high temperatures: implications for 520 km discontinuity, *Phys. Earth Planet. Int.*, **136**, 41–66, 2003.

Vidale, J. E. and H. M. Benz, Upper-mantle seismic discontinuities and the thermal structure of subduction zones, *Nature*, **356**, 678–683, 1992.

Vinnik, L., Detection of waves converted from *P* to *SV* in the mantle, *Phys. Earth Planet. Int.*, **15**, 39–45, 1977.

Walck, M. C., The *P* wave upper mantle structure beneath an active spreading center: the Gulf of California, *Geophys. J. R. Astron. Soc.*, **76**, 697–723, 1984.

Wessel, P. and W. H. F. Smith, New version of the Generic Mapping Tools released, *EOS Trans. Am. Geophys U.*, **76**, 329, 1995.

Wiggins, R. A., G. A. McMechan, and M. N. Toksöz, Range of earth structure nonuniqueness implied by body wave observations, *Rev. Geophys. and Space Phys.*, **11**, 87–113, 1973.

Wright, C., The LSDARC method of seismic refraction analysis: principles, practical considerations and advantages, *Near Surface Geophysics*, **4**, 187–200, 2006.

Wright, C., The *P* wavespeed structure in the upper mantle and transition zone below the western margin of the Philippine Sea plate; geodynamic implications, *Tectonophysics*, 2007 (in press).

Wright, C., K. J. Muirhead, and A. E. Dixon, The *P* wave velocity structure near the base of the mantle, *J. Geophys. Res.*, **90**, 623–634, 1985.

Wright, C., M. T. O. Kwadiba, E. M. Kgaswane, and R. E. Simon, The structure of the crust and upper mantle to depths of 320 km beneath the Kaapvaal craton, from *P* wave arrivals generated by regional earthquakes and mining-induced tremors, *J. Afr. Earth Sci.*, **35**, 477–488, 2002.

Yang, T.-F., T. Lee, C.-H. Chen, S.-N. Cheng, U. Knittel, R. S. Punongbayan, and A. R. Rasdas, A double island arc between Taiwan and Luzon: consequence of ridge subduction, *Tectonophysics*, **258**, 85–101, 1996.

Zhao, M., C. A. Langston, and A. A. Nyblade, Upper mantle velocity structure beneath southern Africa from modeling regional seismic data, *J. Geophys. Res.*, **104**, 4783–4794, 1999.

C. Wright (e-mail: cwrig@earth.sinica.edu.tw) and B.-Y. Kuo